# *Using Distributed Temperature Sensing to monitor field scale dynamics of ground surface temperature and related substrate heat flux*

# Using Distributed Temperature Sensing to monitor field scale dynamics of ground surface temperature and related substrate heat flux

V.F. Bense[+], T. Read[*], A. Verhoef[o]

*Department of Environmental Sciences, Wageningen University, Wageningen, Netherlands*

[*] *School of Environmental Sciences, University of East Anglia, Norwich, UK*

[o] *Department of Geography and Environmental Science, The University of Reading, UK*

[+] *Corresponding Author:* victor.bense@wur.nl
*tel. +31 (0)317 486066*

**Abstract**

We present one of the first studies of the use of Distributed Temperature Sensing (DTS) along fibre-optic cables to purposely monitor spatial and temporal variations in ground surface temperature (GST) and soil temperature, and provide an estimate of the heat flux at the base of the canopy layer and in the soil. Our field site was at a groundwater-fed wet meadow in the Netherlands covered by a canopy layer (between 0-0.5 m thickness) consisting of grass and sedges. At this site, we ran a single cable across the surface in parallel 40 m sections spaced by 2 m, to create a 40×40 m monitoring field for GST. We also buried a short length (≈10 m) of cable to depth of 0.1±0.02 m to measure soil temperature. We monitored the temperature along the entire cable continuously over a two-day period and captured the diurnal course of GST, and how it was affected by rainfall and canopy structure. The diurnal GST range, as observed by the DTS system, varied between 20.94

and 35.08°C; precipitation events acted to suppress the range of GST. The spatial distribution of GST correlated with canopy vegetation height during both day and night. Using estimates of thermal inertia, combined with a harmonic analysis of GST and soil temperature, substrate- and soil-heat fluxes were determined. Our observations demonstrate how the use of DTS shows great promise in better characterising area-average substrate/soil heat flux, their spatiotemporal variability, and how this variability is affected by canopy structure. The DTS system is able to provide a much richer data set than could be obtained from point temperature sensors. Furthermore, substrate heat fluxes derived from GST measurements may be able to provide improved closure of the land surface energy balance in micrometeorological field studies. This will enhance our understanding of how hydrometeorological processes interact with near-surface heat fluxes.
*Keywords:* fibre-optic distributed temperature sensing, temperature, wet meadows, thermal patterns, vegetation structure, energy balance closure

## 1. Introduction

### *1.1. Importance of the land surface thermal regime*

The thermal regime at the land surface is the result of the interactions between vegetation, soil and atmosphere (e.g. transpiration, evaporation, soil water-and heat transfer). These processes are affected by micro-topography, local hydraulic and thermal properties, and radiative and structure parameters, such as canopy height and leaf area index (e.g. Moene and van Dam, 2014; Rodriguez-Iturbe et al., 1999). These complex interactions can be formalized via the energy balance, which is closely related to the water balance

via the evapotranspiration term. The energy balance describes how the net radiation received at the land surface, $R_n$, is distributed between evapotranspiration (latent heat flux, $LE$), sensible heat flux, $H$, and substrate heat flux, $G_{sub}$. The latter flux concerns heat that gets stored in (during the day) or released from (night-time) a substrate layer, consisting of topsoil and leaf-litter.

However, some researchers consider a skin layer heat flux (e.g. Holtslag and de Bruin, 1988; Steeneveld et al., 2006), where the skin layer consists of vegetation, within-canopy air space, leaf litter and top soil, with related effective temperature: the skin temperature. Following a Fourier-type heat transfer law, the skin layer heat flux depends on skin conductivity and the topsoil-skin temperature gradient. Skin conductivity is a complex parameter, that is affected by soil/vegetation thermal properties, within-canopy temperature profiles (affecting canopy heat storage) as well as by within-canopy aerodynamic transfer.

The substrate heat flux, $G_{sub}$, more generally referred to as surface soil heat flux, as both litter layer and canopy layer are often ignored (in particular for short canopies), is a particularly important component of the land-surface energy balance under sparse or heterogeneous canopies. Whereas area-average estimates of the atmospheric fluxes (sensible and latent heat fluxes) can be reliably obtained from eddy covariance measurements, $G_{sub}$ is commonly derived from a small number of point estimates, generally by using soil heat flux plates buried beneath the soil, combined with an estimate of heat storage above the plate, to yield an estimate of heat flux at the soil/substrate surface. Alternatively, $G_{sub}$ can be determined from tempera-

ture measurements at or below the soil surface (e.g. Verhoef, 2004; Verhoef et al., 2012; van der Tol, 2012), as long as estimates of near-surface soil thermal properties are available. These temperatures are generally obtained using in-situ temperature probes installed (just) below the surface (e.g. Mayocchi and Bristow, 1995; Sauer and Horton, 2005). If leaf area index (LAI) varies considerably spatially, surface soil heat (substrate) flux estimates obtained at one or a few locations only may lead to poor energy balance closure ($R_n - G_{sub} \neq H + LE$), which is a widely observed phenomenon (Foken, 2008) that is not only caused by non-representative $G_{sub}$ estimates, but can also be the result of atmospheric phenomena (e.g. advection).

The skin-, or land surface temperature (LST), plays a key role in all four energy balance fluxes. It is generally assumed to be a skin temperature to which the soil/litter layer (i.e. via the ground surface temperature, GST) and all canopy elements contribute, although with most of the signal coming from the top canopy layer. Quantifying the magnitude and spatial distribution of LST is important in micrometeorological and remote sensing studies, with the aim to further our understanding of the intricate functioning of natural or managed ecosystems. For example, through complex feedbacks the land surface thermal regime affects the spatial distribution of fauna and flora, and is a factor in controlling rates of primary production and biogeochemical processes. The spatial patterning of LST within a given habitat may provide thermal refugia for temperature sensitive species, enhancing the resilience of the ecosystem to short-term temperature maxima or minima (e.g. Ashcroft and Gollan, 2013).

LST can be monitored at the large scale using airborne thermal infrared

techniques (e.g. Schmugge et al., 2002; Bertoldi et al., 2010). At an intermediate scale, ground based thermal infrared (IR) thermometers and cameras can be set up to monitor temperature variability over a scale of a few metres (Verhoef, 2004; Pfister et al., 2010), to hundreds of metres (Heinl et al., 2012). However, in the presence of a canopy layer, thermal IR imaging will only provide an effective skin temperature, with the uppermost canopy elements (e.g. sunlit top leaves) contributing most, so no explicit information on GST (i.e. at the base of the vegetation layer) will be available. Furthermore, LST, as well as GST, will be highly variable, in space as well as in time. To address this issue we need sensors that can measure temperatures in a spatially distributed and temporally near-continuous fashion.

Distributed Temperature Sensing (DTS) along fibre-optic cables, installed on the substrate surface or within the soil, provide a convenient means to obtain information on (the variability of) substrate and soil temperatures, e.g. for the verification of (below- and above-ground) multi-component soil-vegetation-atmosphere-transfer (SVAT) model outputs (e.g. Verhoef and Allen, 2000) for which separate measurements of vegetation and soil surface/substrate temperatures are required. Furthermore, line-averaged $G_{sub}$ estimates, if the DTS temperature measurements are combined with measurements or estimates of thermal properties as mentioned above, would allow improved calculations of flux-partitioning when sensible heat flux is derived from scintillometry (Evans et al., 2012), whereas area-averaged estimates of $G_{sub}$ (by using a horizontal multi-loop configuration) are more representative of flux tower footprint areas, and hence these are expected to lead to better energy balance closure than point-scale measurements with

standard soil heat flux equipment. Hence, this paper aims to demonstrate the use of DTS technology in the determination of the spatio-temporal dynamics of soil- and near surface heat fluxes, and our purpose is not to advance the technology of DTS itself. As far as we are aware DTS has not been used for calculations of soil heat flux nor used to illustrate the implications of using a single measurement point as is practised widely in energy balance studies using a single heat flux plate (e.g. Wilson et al., 2002), to obtain soil heat flux for the determination of energy balance closure in heterogeneous canopies.

### *1.2. Distributed Temperature Sensing for monitoring ecosystem temperatures*

Distributed Temperature Sensing (DTS) is being increasingly used for environmental temperature monitoring between the point and regional scale (e.g. Selker et al., 2006). DTS provides temperature measurements along an optical fibre at spatial intervals typically of around 1 m or less and temporal intervals of less than 1 minute. The optical fibre can be configured into almost any spatial pattern such that a two- or three-dimensional space can be monitored for temperature from a single device. This approach, therefore has the potential to bridge the gap between point measurements which provide good temporal but poor spatial information, and remotely captured data which provide detailed spatial measurements but often poor temporal information. Furthermore, one continuous length of DTS cable can be partly placed on the soil and in the substrate, and within the canopy (at different heights, including near the canopy top to emulate IR-derived surface temperatures), thereby providing detailed information on GST and within-canopy temperature profiles, respectively.

The principle behind DTS is that a laser pulse is directed into a fibre optic

cable and the intensity of backscattered photons arising from temperature dependent Raman scattering detected subsequently. Some photons return at higher frequencies, while others return at a lower frequencies. These are known as the anti-Stokes and Stokes intensities, respectively. The temperature, which more strongly affects the anti-Stokes signal, is computed from the ratio of these two intensities. For a more detailed explanation of the fundamental physical principles of the DTS method the reader is referred to Tyler et al. (2009).

A few examples exist of studies deploying DTS for monitoring temperature in natural or managed ecosystem applications. Krause et al. (2012) deployed DTS to investigate the extent to which invasive Rhododendron in a UK woodland modifies canopy temperatures. Similarly, Lutz et al. (2012) measured ground surface temperatures using DTS in both thinned and unthinned forests. In both cases the presence of a canopy was found to significantly moderate the ground surface temperature. These studies look at temperature along transects of cables; however, a two-dimensional configuration in the vertical was utilized by Thomas et al. (2011) to monitor atmospheric-surface layer flows by attaching the optical cable to a frame and system of pulleys. This type of approach (in the horizontal) is to our knowledge yet to be attempted for the monitoring of GST and the derivation of heat fluxes. To demonstrate how DTS can be used to map GST in relatively low canopies, how these temperatures are affected by canopy structure, and how such data can be used to obtain estimates of the spatiotemporal variation of substrate- and soil heat fluxes, we deployed a DTS system in a groundwater-fed meadow in the Netherlands.

## 2. Materials and methods

### *2.1. Field site and measurements of ground surface temperatures with DTS*

The field site of De Maashorst Nature Reserve is located approximately 2 km southwest of the town of Uden in the southeast of the Netherlands (Figure 1a). The site has a high ecological value and is an example of a groundwater-fed wet meadow. A shallow (<1 m) water table is maintained by the Peel Boundary Fault to the southwest of the site (Figure 1b), which acts as a barrier to lateral groundwater flow (in this case, from northeast to southwest). The resultant strong vertical hydraulic gradient, and highly heterogeneous Quaternary cover sands, combine to give localised seepage, visible in aerial photographs of nearby cultivated fields and readily detectable in the agricultural drainage network of the area using temperature-based and hydrochemical methods (Bense and Kooi, 2004; Bonte et al., 2013).

At the study site, these localised seepage phenomena have resulted in a highly variable spatial distribution of plant species. Some regions are dominated by plants adapted for very moist conditions and are densely vegetated by for instance Reed Mannagrass (*Glyceria maxima*), Tufted Sedge (*Carex acuta*), Lesser Pond Sedge (*Carex acutiformis*), Marsh Horsetail (*Equisetum palustre*) and Marsh Marigold (*Caltha palustris*). Neighbouring areas can have much shorter and more sparse vegetation, including Churchyard Moss (*Rhytidiadelphus squarrosus*), Pointed Spear Moss (*Calliergonella cuspidate*), Calliergon Moss (*Calliergon cordifolium*), Thread Rush (*Juncus Filiformis*), and Soft Rush (*Juncus effusus*), reflecting a greater depth to groundwater. In these systems the GST can be expected to be highly spatially organised, and be controlled by the structure (density, height and LAI) of the vegeta-

tion cover through variation in light extinction, as well as by its radiative, thermal and aerodynamic properties that affect the overall energy balance.

To measure the ground surface temperature, approximately 900 m length of steel armoured multimode fibre-optic cable (manufactured by Brugg Cables, *http://www.bruggcables.com*) was used. The fibre-optic cable we used had an outer blue polyutherane jacket. This cable was laid out in a field directly adjacent to the Peel boundary fault zone (Figure 1b). Here, fire-optic cable was installed in 21 parallel sections of 40 m length, with a 2 m spacing between each line. We refer to this area as the *monitoring field*. The cable was loosely secured to the ground, approximately every 2 metres. This resulted in the cable sitting at slightly variable heights above the soil surface (Figure 1c), estimated to be ranging between 0-10 cm. A ≈10 meter long section (Figure 1b; *buried cable section*) was buried to a depth of 10±2 cm, and at the surface a parallel section of cable was installed of roughly equal length (Figure 1d).

Temperature data were collected along the DTS cable continuously over a 48 hour period (25-Aug and 26-Aug, 2009) using an Oryx DTS (Sensornet, Herts, UK), powered by a battery pack and charged by a solar panel. Data along the buried cable section were only collected on 26-Aug. Measurements were obtained over 1.01 metre intervals along the cable with an integration time of 2.5 minutes, using a double-ended configuration (see van de Giesen et al. (2012) for a full explanation and description of the principle of double-ended DTS measurements). Using the double-ended DTS configuration a correction was made to the raw data for the differential attenuation of light along the fibre. To account for temperature offset and instrument drift, a

20 m section of coiled cable and a reference PT100 probe were placed in an insulating box filled with water. The DTS data were subsequently post-processed by comparing the average DTS coil temperature with the PT100 probe, and applying a time-varying offset. A second PT100 probe was placed in the centre of the field adjacent to the cable to validate the calibration procedure. Although the DTS derived temperatures were calibrated, following the procedure outlined above, it is likely that some discrepancies will still exist between ambient temperatures and those sensed along the fibres in the cable. This is due to heat absorption of the cable as a result of solar heating. Consequently, DTS temperatures can be higher than ambient during sunny periods of the day, whilst the magnitude of this effect is dependent on cable colour and thickness (de Jong et al., 2015). For the blue cable (diameter: 4 mm) we use in this study this bias might amount to upto 1-2 $^{o}$C.

The variation in vegetation height was measured manually using a yard-stick, to the nearest 5 cm, at 2 m intervals within the monitoring field. We consider that the vegetation height, albeit being a simple variable, should reflect well the LAI.

Meteorological data including air temperature and precipitation were obtained at hourly intervals from a weather station at Volkel, located at a distance of 6 km from the field site. At the field site, no meteorological data were collected.

### *2.2. Calculation of substrate- and soil heat flux from DTS measurements*

We consider the *substrate* as that zone directly surrounding the above-ground DTS cable in the monitoring field where heat is stored in/released from and transferred to/from a substrate consisting of soil, above ground

litter and fresh leaf matter and air (Figure 1e). We employ the term *soil* in the conventional way and used the soil temperatures as measured in the buried cable section to calculate a soil heat flux at the depth of cable burial and the GST measurements to derive substrate heat flux.

The original 2.5 minute averaged DTS temperature were averaged to give 30-minute average temperature values for each 1.01 m along the DTS cable. The temperature measurements were subjected to a harmonic analysis, which allowed calculation of substrate- and soil heat flux ($G_{sub}$ and $G_{soil}$), using one estimate of average substrate thermal properties across the entire monitoring field, and that of the soil along the length of buried cable, respectively. We recognise that the thermal properties of the substrate and soil will be spatially variable, but we did not quantify this variability at our field site. For the soil, the texture and moisture content over a site will vary to a certain degree but at soil moisture contents above 50% of saturation (see Murray and Verhoef (2007a)) this sensitivity is very strongly reduced. At our site with very shallow groundwater tables it is likely that soils are near saturation. Nevertheless, soil thermal properties could have been determined by using a heat-pulse needle probe, but substrate properties would have been impossible to obtain in this way due to lack of contact between probe and the bulk of the substrate, and there is currently no way of routinely obtaining such data in the field. We accept that for some locations we will overestimate/ or underestimate heat fluxes by assuming spatially constant thermal properties. However, we expect that the overall variability in heat fluxes would not change significantly if the detailed variability in thermal properties would have been known. This is because the biggest determinant

of variability in diurnal peak value in heat fluxes is the amplitude of temperature which will be most strongly influenced by parameters like canopy properties, such as height and density, causing variations in shading, and within-canopy and near soil-surface aerodynamic resistances. Furthermore, high moisture contents in the capillary fringe and moisture fluxes due to root water uptake may affect the ground surface temperatures, but these effects are implicit in the temperature fluctuations and spatial distributions of temperature, hence they are already implicitly included in the soil heat flux as it is calculated following the methodology outlined below.

Substrate- and soil heat fluxes were calculated using the method described in Verhoef (2004) and Murray and Verhoef (2007b). This involved a harmonic analysis of DTS temperatures, which was followed by calculation of the heat flux $G$ [W m$^{-2}$] using an analytical method. This approach requires the estimation of thermal inertia ($\Gamma$ [J m$^{-2}$ K$^{-1}$ s$^{-0.5}$]) for both the soil and the substrate. $\Gamma$ is defined as $\sqrt{\lambda C_h}$ where $\lambda$ [W m$^{-1}$ K$^{-1}$] is thermal conductivity, and $C_h$ [J m$^{-3}$ K$^{-1}$] is volumetric heat capacity.

The soil type at the field site was peat and typical values of peat thermal properties were selected from the literature. For $C_h$, a value of $3{\cdot}10^6$ J m$^{-3}$ K$^{-1}$ was selected and thermal diffusivity, $D_h$, equalled $1.1{\cdot}10^{-7}$ m$^2$ s$^{-1}$ (near-saturation values derived from Table 1.2.4 in Grossnickle (2000)) which led to a thermal conductivity ($D_h C_h$) of 0.33 W m$^{-1}$ K$^{-1}$. In turn, this resulted in an estimate for soil thermal inertia, $\Gamma_{soil}$, of 995 J m$^{-2}$ K$^{-1}$ s$^{-0.5}$, which was used for the calculation of soil heat flux ($G_{soil}$), based on below ground DTS measurements.

However, the substrate also consisted of grass and air as it was impos-

sible at the field site to have the fibre-optic cable touching the ground or leaf/litter surfaces throughout the entirety of its length. Nevertheless, this set-up provides a good approximation of the skin layer heat flux, as introduced in Section 1.1. With $C_h$ for grass equal to $2.8{\cdot}10^6$ J m$^{-3}$ K$^{-1}$ (which is similar to peat) and $\lambda$= 1.1 W m$^{-1}$ K$^{-1}$ (Yaghoobian et al., 2010), we found $\Gamma$=1755 J m$^{-2}$ K$^{-1}$ s$^{-0.5}$, whereas thermal inertia for air is 5.5 J m$^{-2}$ K$^{-1}$ s$^{-0.5}$. From visual estimates in the field we assume a substrate composition of about 35% air, 40% grass and 25% soil over each meter length of cable, $\Gamma_{substrate}$= 955 J m$^{-2}$ K$^{-1}$ s$^{-0.5}$.

With an estimate of thermal inertia we obtain a value for $G$ using:

$$G = \Gamma \sum_{n=1}^{M} A_n \sqrt{n\omega} \left[ sin[n\omega t + \phi_n + \frac{\pi}{4}] \right] \quad (1)$$

where $M$ is the total number of harmonics ($n$) used (20), $A_n$ [$^o$C] the amplitude of the $n^{th}$ harmonic, $\phi_n$ the phase shift of the $n^{th}$ harmonic, $t$ [s] the time and $\omega$ is the angular frequency ($24{\times}60{\times}60$ $s$). $A_n$ and $\phi_n$ are derived from the harmonic analysis of DTS temperatures.

## 3. Results

### *3.1. Temporal Ground Surface Temperature dynamics*

The two full days (25-Aug and 26-Aug) covered by DTS measurements had contrasting meteorological conditions. On 25-Aug, rainfall overnight was followed by further rainfall approximately between 10:00 and 12:00 hrs (Figure 2a). This totalled only 0.2 mm at the Volkel meteorological station. From 12:00 hrs, there was no further precipitation recorded at Volkel. The

following day (26-Aug) was relatively warm and had been preceded by a cold night.

Figure 2b plots the mean and range in GST across the monitoring field, as observed by DTS. Comparing these time series to those of air-temperature (Figure 2a) shows that GST varies in a way similar to air temperature. Note that prior to the rainfall event on the 25-Aug, the GST is consistently below the air temperature at Volkel, and has a relatively small range (Figure 2b). From approximately 20:00 on 25-Aug, the range in GST is in general much larger, except around 08:00 and 20:00 hrs when it reaches a minimum. Furthermore, the absolute value of GST is almost always higher than the air temperature during the day and lower at night.

### *3.2. Spatial and temporal dynamics during warming*

In order to investigate the spatiotemporal dynamics of GST across the monitoring field we selected two sequences from the entire data set. We consider the daytime temperature dynamics following the rainfall event on 25-Aug (between 10:00 hrs and 12:00 hrs), and compare this with the warming recorded during the morning of the following day with antecedent dry conditions. For every location along the cable, the difference in temperature ($\Delta$GST), was calculated relative to the spatially averaged GST at reference times ($t_0$; Figure 2a) of 12:25 hrs and 08:35 hrs on the 25th and 26th Aug, respectively. Values of $\Delta$GST were calculated at four times ($t_{1-4}$ after $t_0$, separated by 25 minutes, on both days. The $\Delta$GST values were then spatially mapped onto a grid with 2 m spacing in the O-X direction, and 1 m spacing in the O-Y direction to replicate the spatial sampling interval in the field.

Figure 3 shows the spatially mapped ΔGST values at the four times after $t_0$ on 25-Aug (a-d), and 26-Aug (e-h). On 25-Aug, there is little change in GST after the first 25 minutes. After this, both the range and mean ΔGST have increased - a trend which continues until 14:05 hrs. By now there is a spatial organisation to the ΔGST which correlates with the vegetation height; the vegetation height is shown on each plot using contour lines. This correlation is further illustrated in Figure 4. Those areas with the shortest vegetation, and hence with the lowest LAI, experience the greatest warming. On 26-Aug the initial warming is more rapid, and by 10:15 hrs there exists a pattern of ΔGST similar to that in vegetation height.

### *3.3. Impact of vegetation on GST dynamics*

To investigate the effect of variable vegetation cover on the temperature dynamics, each DTS temperature measurement location was assigned to one of six groups according to vegetation height at that point. The group ranges were chosen such that the number of samples ($n$) in each group was as equal as possible, whilst still maintaining a distinct group which had the tallest vegetation only. The time series of average GST for each group was calculated, and the mean field temperature then subtracted to give the difference from the mean GST for each group (Figure 4).

A clear diurnal signal emerges; areas with the lowest canopy height (<5 cm) are colder at night and warmer during the day, than those areas with tall (50-90 cm) vegetation (Figure 4a). A transition, where the total range of GST is low, and the tallest vegetation regions switch from being the coldest to being the warmest regions, occur at 20:00 hrs on both days. The reverse happens at around 08:00 hrs on 26-Aug and to a lesser extent at around

the same time on the previous day. The magnitude of the daytime vegetation shading effect is much reduced on 25-Aug, due to increased cloud cover which means there is less direct radiation reaching the canopy. A prevalence of diffuse radiation will lead to much less pronounced differences in GSTs between low and high crop height/LAI areas. In contrast, on a sunny day there would be distinct sunlit and shaded areas, due to considerable differences in radiation extinction, which is highly affected by LAI.

The presence of taller plant species has a clear moderating effect on the variation in GSTs. During Aug 26, at any point in the monitoring field the maximum of the range of diurnal GST variations was 35.08 °C while the minimum was 20.94 °C (Figure 4b). The temperature range visually strongly correlates with the vegetation height ($r^2$=0.48), and is greatest where there is little or no vegetation cover.

Figure 5 shows the observed temperatures in the buried cable section for 26-Aug. The temperatures along the cable show clearly where the cable enters the soil (Figure 5a) at which point a transition zone occurs in which the temperatures recorded are in between those recorded at the surface (substrate) and in the soil (soil) (Figure 5b). The data show that the spatial variation of temperature within each section (substrate and soil) is fairly low and varies slightly over time.

### *3.4. Substrate- and soil heat flux dynamics*

The calculated spatiotemporal trends in substrate- and soil heat flux ($G_{sub}$ and $G_{soil}$, respectively) are discussed for 26-Aug only, a day with a more clearly defined diurnal temperature signal than 25-Aug. Moreover, data for the buried cable section are only available for 26-Aug.

Figure 6 shows the evolution of the calculated $G_{sub}$ for 26-Aug (a predominantly sunny day, but with broken cloud occurrences in the afternoon) spatially averaged across the monitoring field, together with the $G_{soil}$ in the buried section. Following standard behaviour of substrate and soil heat fluxes $G_{sub}$ and $G_{soil}$ vary diurnally, with negative values during the night and positive values between sunrise and sunset. For $G_{sub}$ this denotes ground surface heat loss to and heat gain from the in-canopy air space, respectively; for $G_{soil}$ these negative and positive fluxes are representative of heat loss to and heat gain from the soil layer above the below-ground DTS installation depth.

The magnitude of the substrate soil heat flux (peak value of around 190 W $m^{-2}$) fits with 26-Aug being a warm, predominantly sunny day and the substrate being relatively exposed (crop height <0.5 m and low LAI from visual inspection). Values of $G_{sub}$ at their maximum (around 11:00 hrs) ranged between 84 $Wm^{-2}$ to 190 $Wm^{-2}$ with an average of 150 $Wm^{-2}$, whereas for $G_{soil}$ values between 25 and 46 $Wm^{-2}$ were found (average of 39 $Wm^{-2}$). The soil heat flux values in the buried cable section peak around 12:00 hrs whilst the mean substrate heat fluxes across the field peaks earlier at 10:30-11:00 hrs. This reflects standard behaviour where the amplitude of diurnal variability is dampened in the soil, and a delay of peak values occurs.

Figure 6b-d shows values of $G_{sub}$ for 26-Aug, overlain by contours of vegetation height, to illustrate how $G_{sub}$ varies considerably over the monitoring field over the duration of a day. Early in the day, at 05:00 hrs (Figure 6b), all calculated $G_{sub}$ values are negative indicating that the substrate is cooling. The more exposed areas are cooling more rapidly, indicated by a more negative $G_{sub}$ in those parts of the field. At 11:00 hrs when values peak

(Figure 6c), the latter pattern is inverted to a degree where at this time of day the more exposed areas display the higher $G_{sub}$ values. This is to be expected as the places where the canopy is sheltering the soil to a lesser degree, will have received more radiation and hence will exhibit larger substrate heat fluxes. Later in the day at 17:00 hrs (Figure 6d) a similar pattern of $G_{sub}$ arises as was present in the morning arises indicating that more exposed areas are cooling more rapidly than secluded areas. It is noticeable that in the afternoon of 26-Aug the mean and range in $G_{sub}$ are strongly fluctuating at a time-scale of hours alternating between mean average and positive values. These can not be directly attributed to fluctuations in air-temperature, which do not display such variability (Figure 2), and most likely coincide with variations in incoming radiation.

## 4. Discussion and Conclusions

We deployed Distributed Temperature Sensing to monitor near surface temperatures in a wet meadow site in the Netherlands, in the late summer season. Using a relatively simple cable configuration, we were able to map considerable temperature patterns in great spatio-temporal detail. Temperature data like these, as we collected using DTS, would be practically impossible to collect with any other field methodology. In the discussion of our results we aim to separate spatial patterns and temporal dynamics present in our data.

The emerging spatial trends in the temperature data correlate with vegetation height, in particular, when the diurnal range of temperatures is considered (Figure 4b), as well as for the calculated substrate heat fluxes (Fig-

ure 6b-d). For taller vegetation, diurnal GST and $G_{sub}$ variations are significantly smaller indicating that the thicker canopy more effectively dampens air temperature fluctuations. This results in temperatures that are higher underneath thicker vegetation during the night but relatively cool during day-time (Figure 4a). These spatiotemporal differences in the diurnal range of GST and $G_{sub}$ are a combination of radiative, aerodynamic and thermodynamic effects. Examples are a reduction in direct solar radiation (via canopy radiative extinction) received during the day and prevention of radiative cooling via long-wave outgoing radiation, and substrate heat loss driven by a temperature gradient between soil and substrate temperature, at night. When precipitation events occur these are observed to have an immediate temperature homogenizing effect which is largely independent of vegetation height (Figure 2 and 3). This likely is the result of evaporation of intercepted water and the fact that radiation will be predominantly diffuse during and just after rainfall. Our data set allowed us to illustrate how the substrate surface temperature distribution evolves from such thermally homogeneous conditions which can either be caused by a rainfall event (Figure 3a-d) or from the presence of dew in combination with the impact of diurnal incoming radiation temperature dynamics (Figure 3e-h).

In future studies, the collection of on-site auxillary data such as meteorological and independent heat flux observations will aid to understand correlations between observed temperature distributions and meteorological and soil conditions. However, we emphasize that if such measurements at selected locations are obtained their use would be hampered by a series of issues. Temperature measurements with thermocouples or IR thermometers

have their own particular problems such as radiation effects/contact issues with thermocouples, or lack of surface emissivity data for IR measurements. Furthermore, independent measurements of soil heat flux using soil heat flux plates should not be viewed as a standard or reference method. They suffer as well from a range of shortcomings, such as interference with soil moisture flow, contact problems, and inaccuracies in the calculation of above-plate heat storage. These limitations reduce the usability of such data for the the interpretation, or validation, of DTS derived temperatures and associated heat fluxes.

The DTS technique illustrated here also shows great promise in getting a better handle on area-average substrate and below-ground soil heat flux estimates, and their spatio-temporal variability, when the temperature measurements are combined with a harmonic analysis and subsequent calculation of soil heat flux with an analytical method (Verhoef, 2004). It seems that the heat flux directly at or below the soil surface can be obtained from DTS cables placed at the soil surface or buried in the soil, but the installation needs to be conducted very carefully. That is, the cable is either secured right against the soil/litter layer surface or the below-ground installation depth is known with as high a precision as possible. Verhoef (2004) and van der Tol (2012) have shown that the *surface* soil heat flux derived from soil temperatures, which requires a more complex analytical equation than Eq. 1 (see Verhoef, 2004: Eq. 6 and Verhoef et al., 2012: Eq. 9) that uses $C_h$ and $D_h$ explicitly (rather than the composite thermal property, $\Gamma$), as well as the distance between the measurement location and the soil surface, is very sensitive to errors in the assumed installation depth. Furthermore, it would be

preferable to install further parts of the cable at different heights throughout the canopy so that estimates of canopy heat storage can be obtained in the context of skin layer conductivity/skin layer heat transfer (see Section 1.1). Knowledge of the heat exchanged with or stored within the canopy would lead to significantly reduced errors in energy balance closure (Moderow et al., 2009).

We conclude that our DTS measurements have captured the temperature dynamics resultant from soil-vegetation-atmosphere energy exchanges in great spatial and temporal detail. However, in the absence of further experimental data such as field-average net radiation and sensible and latent heat fluxes, or within-field variation in leaf temperatures, it is not possible to evaluate the relative importance of different heat fluxes in this ecosystem, and interpret the DTS data in more detail, for example using SVAT modeling. In addition to the monitoring of these variables and fluxes in future studies, the DTS component can be expanded to include sections where the cable is buried into the soil, in order to potentially capture soil moisture dynamics as pioneered by Steele-Dunne et al. (2010). Shading effects could be further evaluated by using white and black jacketed fibre-optic cables in a similar way as described by Petrides et al. (2011) who studied shading over stream channels using DTS.

Also, in the present study, we only look at two-dimensional spatial variation in temperature. However, it is possible to configure the cable such that any geometry in space may be monitored. This could be made to include the soil, canopy, and above canopy at a number of different heights. It is also possible, by coilling the fiber optic cable around a vertical cylinder, for exam-

ple, to increase the effective spatial resolution (e.g. Vogt et al. (2010) for a stream bed and van Emmerik et al. (2013) for a lake application). When considering the energy balance at the land surface, and in particular the role of within-canopy storage, several of these high resolution vertical profiles could be included, as part of the same fibre optic cable.

Moreover, ground based- (e.g. Cardenas et al., 2008; Pfister et al., 2010) or airborne thermal imaging (e.g. Richter et al., 2009), mostly capturing the temperature of surface elements at or near the top of the canopy, can be combined with DTS which in our set-up monitors temperatures inside the canopy. This may lead to more accurate estimates of sensible heat flux when this flux is determined from bulk transfer equations, that rely on a surface-air temperature gradient. Although our field campaign was limited to only a few days at the end of the summer season (late August); longer term monitoring would yield further information on the temperature effects of vegetation dynamics in terms of the energy balance, but also in the context of soil respiration, for example, as this is strongly affected by seasonal changes in soil temperature and presence of vegetation (vigorous root growth/respiration during summer, versus winter vegetation dormancy with microbial respiration only). All of these efforts would further our understanding of the interactions between near-surface heat flow dynamics and ecohydrological processes.

## Acknowledgements

Nico Ettema of the Institute for Nature Education and Sustainability, Uden, Netherlands is thanked for valuable advice during field work.

## References


Ashcroft, M. B., Gollan, J. R., 2013. Moisture, thermal inertia, and the spatial distributions of near-surface soil and air temperatures: Understanding factors that promote microrefugia. Agricultural and Forest Meteorology 176, 77–89.

Bense, V. F., Kooi, H., 2004. Temporal and spatial variations of shallow subsurface temperature as a record of lateral variations in groundwater flow. Journal of Geophysical Research B: Solid Earth 109 (4).

Bertoldi, G., Notarnicola, C., Leitinger, G., Endrizzi, S., Zebisch, M., Della Chiesa, S., Tappeiner, U., 2010. Topographical and ecohydrological controls on land surface temperature in an alpine catchment. Ecohydrology 3 (2), 189–204.

Bonte, M., Geris, J., Post, V., Bense, V., van Dijk, H., Kooi, H., 2013. Mapping surface water-groundwater interactions and associated geological faults using temperature profiling. Vol. Groundwater and Ecosystems of IAH Series on Hydrogeology. Ch. Chapter 8, pp. 81–94.

Cardenas, B., Harvey, J., Packman, A., Scott, D., 2008. Ground-based thermography of fluvial systems at low and high discharge reveals potential complex thermal heterogeneity driven by flow variation and bioroughness. Hydrological Processes 22.

de Jong, S. A. P., Slingerland, J. D., van de Giesen, N. C., 2015. Fiber optic distributed temperature sensing for the determination of air temperature. Atmospheric Measurement Techniques 8, 335–339.

526 Evans, J. G., McNeil, D., Finch, J. W., Murray, T., Harding, R. J., Ward,
527 H., Verhoef, A., 2012. Determination of turbulent heat fluxes using a large
528 aperture scintillometer over undulating mixed agricultural terrain. Agri-
529 cultural and Forest Meteorology (166-167), 221–233.

530 Foken, T., 2008. The energy balance closure problem: an overview. Ecological
531 Applications 18, 1351–1367.

532 Grossnickle, S., 2000. Ecophysiology of Northern Spruce Species: The Per-
533 formance of Planted Seedlings. NRC Research Press.

534 Heinl, M., Leitinger, G., Tappeiner, U., 2012. Diurnal surface temperature
535 regimes in mountain environments. Physical Geography 33 (4), 344–359.

536 Holtslag, A. A. M., de Bruin, H., 1988. Applied modelling of the night-time
537 surface energy balance over land. Boundary-Layer Meteorology (27), 689–
538 704.

539 Krause, S., Taylor, S. L., Weatherill, J., Haffenden, A., Levy, A., Cassidy,
540 N. J., Thomas, P., 2012. Fibre-optic distributed temperature sensing for
541 characterizing the impacts of vegetation coverage on thermal patterns in
542 woodlands. Ecohydrology.

543 Lutz, J. A., Martin, K. A., Lundquist, J. D., 2012. Using Fiber-Optic Dis-
544 tributed Temperature Sensing to Measure Ground Surface Temperature in
545 Thinned and Unthinned Forests. Northwest Science 86 (2), 108–121.

546 Mayocchi, C., Bristow, K., 1995. Soil surface heat flux: some general ques-
547 tions and comments on measurements. Agricultural and Forest Meteorol-
548 ogy 75, 43–50.

549 Moderow, U., Aubinet, M., Feigenwinter, C., Kolle, O., Lindroth, A., Molder,
550 M., Montagnani, L., Rebmann, C., Bernhofer, C., 2009. Available energy
551 and energy balance closure at four coniferous forest sites across Europe.
552 Theoretical and Applied Climatology, 98 (3-4), 397–412.

553 Moene, A., van Dam, J., 2014. Transport in the Atmosphere-Vegetation-Soil
554 Continuum. Cambridge University Press.

555 Murray, T., Verhoef, A., 2007a. Moving towards a more mechanistic ap-
556 proach in the determination of soil heat flux from remote measurements i.
557 a universal approach to calculate thermal inertia. Agricultural and Forest
558 Meteorology (147), 80–87.

559 Murray, T., Verhoef, A., 2007b. Moving towards a more mechanistic approach
560 in the determination of soil heat flux from remote measurements ii. diurnal
561 shape of soil heat flux. Agricultural and Forest Meteorology (147), 88–97.

562 Petrides, A., Huff, J., Arik, A., van de Giesen, N., Kennedy, A. M., Thomas,
563 C. K., Selker, J. S., 2011. Shade estimation over streams using distributed
564 temperature sensing. Water Resour. Res. 47, W07601.

565 Pfister, L., McDonnell, J. J., Hissler, C., Hoffmann, L., 2010. Ground-based
566 thermal imagery as a simple, practical tool for mapping saturated area
567 connectivity and dynamics. Hydrological Pro 21, 3123–3132.

568 Richter, K., Palladino, M., Vuolo, F., Dini, L., D'Urso, G., 2009. Spatial
569 distribution of soil water content from airborne thermal and optical remote
570 sensing data. Proceedings of SPIE - The International Society for Optical
571 Engineering 7472.

572 Rodriguez-Iturbe, I., D'Odorico, P., Porporato, a., Ridolfi, L., 1999. On the
573 spatial and temporal links between vegetation, climate, and soil moisture.
574 Water Resources Research 35 (12), 3709.

575 Sauer, T. J., Horton, R., 2005. Soil heat flux. In: Micrometeorology in Agri-
576 cultural Systems. Vol. 47 of Agronomy Monograph. Ch. 7, pp. 131–154.

577 Schmugge, T., Kustas, W., Ritchie, J., Jackson, T., Rango, A., 2002. Remote
578 sensing in hydrology. Advances in Water Resources 25 (8-12), 1367–1385.

579 Selker, J., Thévenaz, L., Huwald, H., Mallet, A., Luxemburg, W., Van
580 De Giesen, N., Stejskal, M., Zeman, J., Westhoff, M., Parlange, M., 2006.
581 Distributed fiber-optic temperature sensing for hydrologic systems. Water
582 Resources Research 42 (12).

583 Steele-Dunne, S., Rutten, M., Krzeminska, D., Hausner, M., Tyler, S., Selker,
584 J., Bogaard, T., Van De Giesen, N., 2010. Feasibility of soil moisture es-
585 timation using passive distributed temperature sensing. Water Resources
586 Research 46, W03534.

587 Steeneveld, G., van de Wiel, B., Holtslag, A., 2006. Modeling the evolution
588 of the atmospheric boundary layer coupled to the land surface for three
589 contrasting nights in cases-99. J. Atmos. Sci. (63), 920–935.

590 Thomas, C. K., Kennedy, A. M., Selker, J. S., Moretti, A., Schroth, M. H.,
591 Smoot, A. R., Tufillaro, N. B., Zeeman, M. J., Nov. 2011. High-Resolution
592 Fibre-Optic Temperature Sensing: A New Tool to Study the Two-
593 Dimensional Structure of Atmospheric Surface-Layer Flow. Boundary-
594 Layer Meteorology, 177–192.

595 Tyler, S. W., Selker, J. S., Hausner, M. B., Hatch, C. E., Torgersen, T.,
596 Thodal, C. E., Schladow, S. G., Jan. 2009. Environmental temperature
597 sensing using Raman spectra DTS fiber-optic methods. Water Resources
598 Research 45, 1–11.

599 van de Giesen, N., Steele-Dunne, S. C., Jansen, J., Hoes, O., Hausner, M. B.,
600 Tyler, S., Selker, J., 2012. Double-Ended Calibration of Fiber-Optic Ra-
601 man Spectra Distributed Temperature Sensing Data. Sensors, 5471–5485.

602 van der Tol, C., 2012. Validation of remote sensing of bare soil ground heat
603 flux. Remote Sensing of Environment 121, 275–286.

604 van Emmerik, T., Rimmer, a., Lechinsky, Y., Wenker, K., Nussboim, S.,
605 van de Giesen, N., 2013. Measuring heat balance residual at lake sur-
606 face using Distributed Temperature Sensing. Limnology and Oceanogra-
607 phy: Methods 11 (1991), 79–90.

608 Verhoef, A., 2004. Remote estimation of thermal inertia and soil heat flux
609 for bare soil. Agricultural and Forest Meteorology 123, 221–236.

610 Verhoef, A., Allen, S., 2000. A SVAT scheme describing energy and $CO_2$
611 fluxes for multi-component vegetation: calibration and test for a sahelian
612 savannah. Ecological Modelling (127), 245–267.

613 Verhoef, A., Ottle, C., Cappelaere, B., Murray, T., Saux-Picart, S., Zribi,
614 M., Maignan, F., Boulain, N., Demarty, J., Ramier, D., 2012. Spatio-
615 temporal surface soil heat flux estimates from satellite data; results for the
616 amma experiment at the Fakara (Niger) supersite. Agricultural and Forest
617 Meteorology 154-155, 55–66.

618 Vogt, T., Schneider, P., Hahn-Woernle, L., Cirpka, O. A., 2010. Estimation
619 of seepage rates in a losing stream by means of fiber-optic high-resolution
620 vertical temperature profiling. Journal of Hydrology 380 (1-2), 154–164.

621 Wilson, K. B., Goldstein, A. H., Falge, E., Aubinet, M., Baldocchi, D.,
622 Berbigier, P., Bernhofer, C., Ceulemans, R., Dolman, H., Field, C., Grelle,
623 A., Law, B., Meyers, T., Moncrieff, J., Mon-son, R., Oechel, W., Tenhunen,
624 J., Valentini, R., Verma, S., 2002. Energy balance closure at FLUXNET
625 sites. Agric. Forest. Meteorology 113, 223–243.

626 Yaghoobian, N., Kleissl, J., Krayenhoff, E., 2010. Modeling the thermal ef-
627 fects of artificial turf on the urban environment. J. Appl. Meteor. Clima-
628 tol. (49), 332–345.

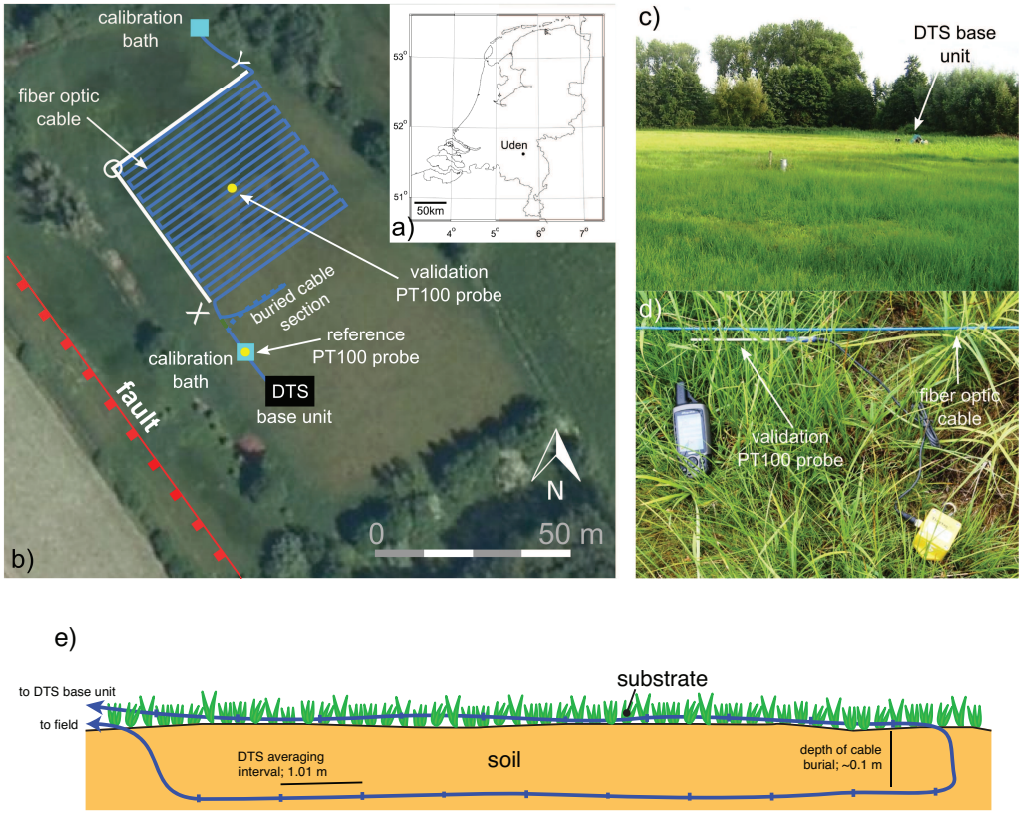


Figure 1: (a) Location of the field site near the village of Uden, Netherlands. (b) The configuration of the DTS monitoring set-up, (c) wet meadow area where the fiber optic cable was deployed, and (d) validation PT100 probe adjacent to the fiber optic cable. (e) Configuration of the buried cable section.

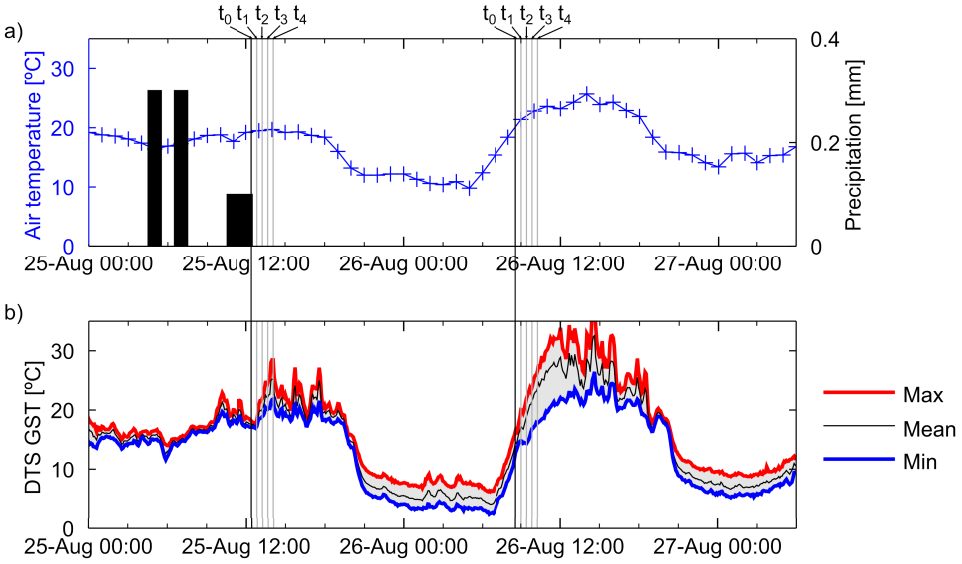


Figure 2: (a) Air temperature and precipitation measured at Volkel, (b) time series of maximum, mean, and minimum GST recorded with the DTS along the fibre optic cable.

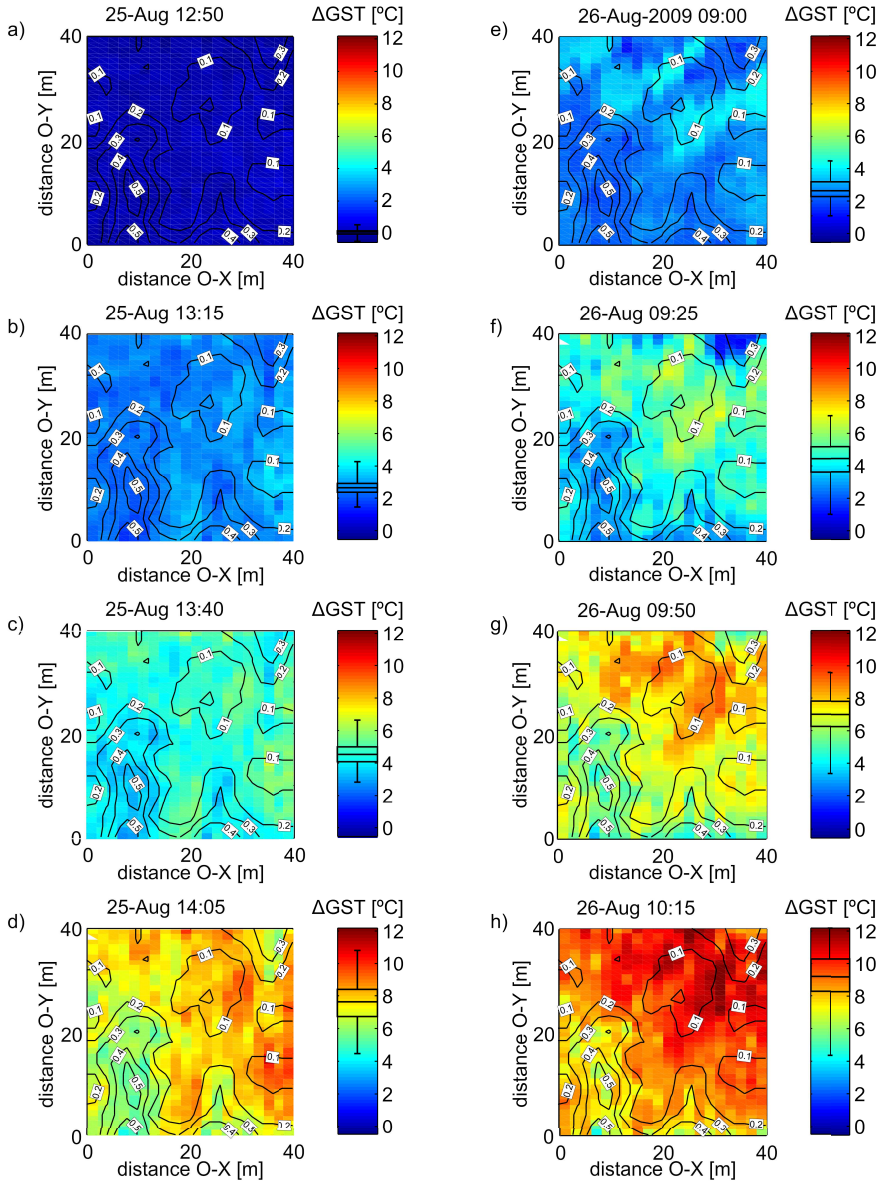


Figure 3: (a-d) ΔGST distribution at 12:50 hrs ($t_1$; Figure 2b), 13:15 hrs ($t_2$), 13:40 hrs ($t_3$), and 14:05 hrs ($t_4$) on 25-Aug, and (e-h) 09:00 hrs ($t_1$) , 09:25 hrs, ($t_2$), 09:50 hrs ($t_3$), and 10:15 hrs ($t_4$) on 26-Aug. Each plot is overlaid with contour plots of the vegetation height [m]. The box plot in each colour bar gives the minimum, lower quartile, median, upper quartile, and maximum ΔGST.

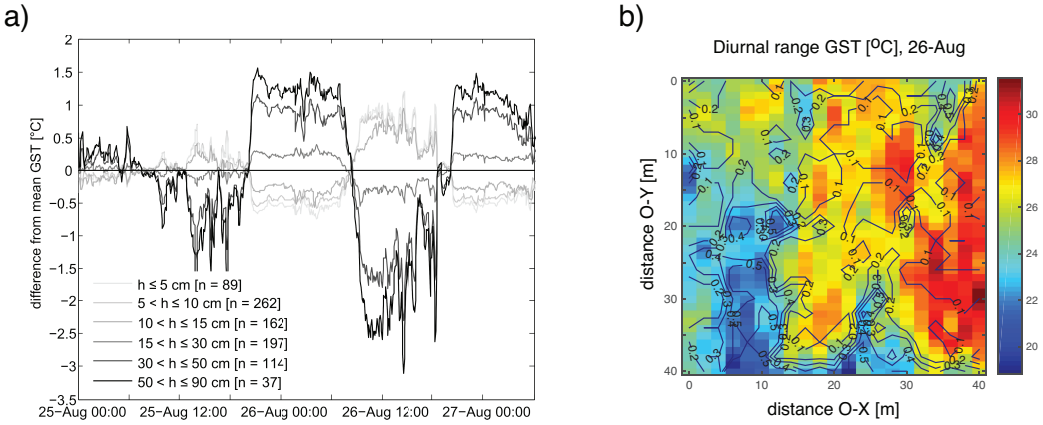


Figure 4: (a) Difference between the mean GST relative to the temporal mean of the monitored area, for different vegetation height groupings. (b) The spatial variability of the diurnal range in GST on 26-Aug. The plot is overlaid with contours of the vegetation height [m].

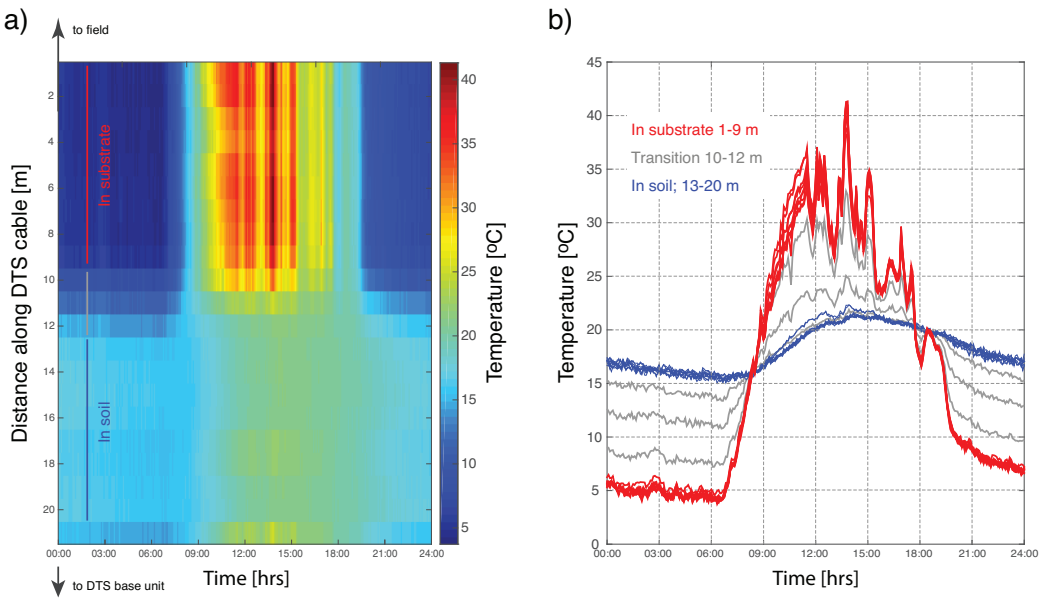


Figure 5: (a) DTS temperature data for the buried cable section on 26-Aug. Location and set-up used to obtain these data are shown in Figure 1a and Figure 1d respectively. (b) DTS temperature in time for each part of the cable in the buried cable section. Data have a time resolution of 2.5 min.

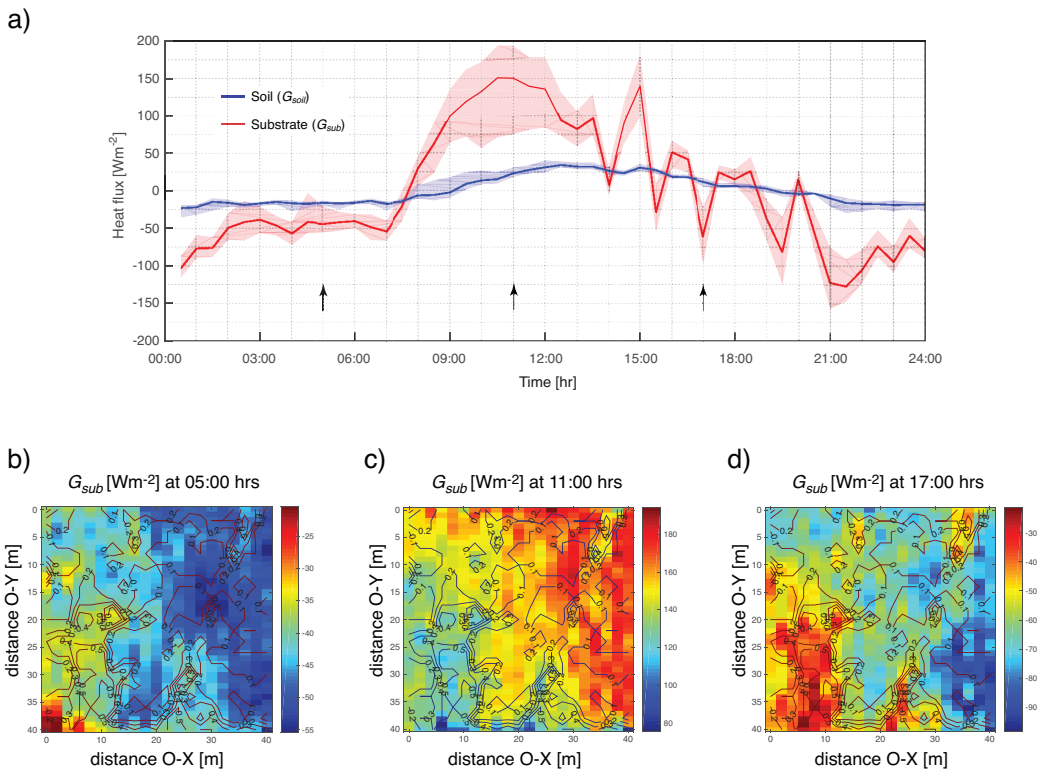


Figure 6: (a) Substrate- and soil heat flux calculated for the field, and the buried cable section respectively, on 26-Aug. The mean heat flux values are indicated by the solid lines, while the range of the observed values is indicated by the shaded area. A total of 860 DTS observations were used to calculate the substrate heat flux at each 30 minute time step, whilst for the soil heat flux in the BG section only 8 DTS observations were available (see Figure 5. The arrows indicate the time steps for which the spatial distribution of the substrate heat fluxes are shown in (b-d). The spatial variability of $G_{sub}$ is shown for (b) 05:00 hrs, (c) 11:00 hrs, and (d) 17:00 hrs. Each plot is overlaid with contours of the vegetation height [m].